Laser and Particle Beams (2010), *28*, 351–359.

doi:10.1017/S0263034610000303

Ion jet generation in the ultraintense laser interactions with rear-side concave target

BIN LIU,[1,2] HUA ZHANG,[1,3] LI-BIN FU,[1,3] YU-QIU GU,[4] BAO-HAN ZHANG,[4] MING-PING LIU,[5] BAI-SONG XIE,[6] JIE LIU,[1,3] AND XIAN-TU HE[1,3]

[1]Center for Applied Physics and Technology, Peking University, Beijing, People's Republic of China
[2]Graduate School, China Academy of Engineering Physics, Beijing, People's Republic of China
[3]Institute of Applied Physics and Computational Mathematics, Beijing, People's Republic of China
[4]Fusion Research Center, Chinese Academy of Engineering Physics, Mianyang, Sichuan Province, People's Republic of China
[5]School of Information Engineering, Nanchang University, Nanchang, People's Republic of China
[6]College of Nuclear Science and technology, Beijing Normal University, Beijing, People's Republic of China

(RECEIVED 7 September 2009; ACCEPTED 8 April 2010)

Abstract

In this paper, the ion jet generation from the interaction of an ultraintense laser pulse and a rear-side concave target is investigated analytically using a simple fluid model. We find that the ion expanding surface at the rear-side is distorted due to a strong charge-separation field, and that this distortion becomes dramatic with a singular cusp shown on the central axis at a critical time. The variation of the transverse ion velocity and the relative ion density diverge on the cusp, signaling the emergence of an on-axis ion jet. We have obtained analytical expressions for the critical time and the maximum velocity of the ion jet, and suggested an optimum shape for generating a collimated energetic ion jet. The above theoretical analysis has been verified by particle-in-cell (PIC) numerical simulations.

Keywords: Ion acceleration; Ion jet; Target-normal sheath acceleration; Ultrashort ultraintense laser

1. INTRODUCTION

The advent of ultrashort ultraintense laser pulses led to the development of new exciting fields in laser plasma interaction (Karsch *et al.*, 1999; Malka *et al.*, 2004; Roth *et al.*, 2005; Mangles *et al.*, 2006; Kawata *et al.*, 2005; Yu *et al.*, 2005; Glowacz *et al.*, 2006; Koyama *et al.*, 2006; Lifshitz *et al.*, 2006; Sakai *et al.*, 2006; Yu *et al.*, 2007; Hora, 2007; Dromey *et al.*, 2009; Fazio *et al.*, 2009; Hoffmann 2008*a*, 2008*b*; Kasperczuk *et al.*, 2009*a*, 2009*b*; Laska *et al.*, 2007; Limpouch *et al.*, 2008; Malekynia *et al.*, 2009; Sharma & Sharma 2009; Izgorodin *et al.*, 2009; Li *et al.*, 2009; Sadighi-Bonabi *et al.*, 2009; Hong *et al.*, 2009; Kline *et al.*, 2009). The generation of energetic ion beams from laser plasma interaction is an exciting area of research with important applications ranging from medical proton therapy (Bulanov & Khoroshkov, 2002), high-energy-density physics (Patel *et al.*, 2003), to fast ignition in inertial confinement fusion (Roth *et al.*, 2001). A beam of energetic ions has an almost straight trajectory while penetrating matter, as well as an excellent coupling efficiency to the nuclear fuel, and delivers its energy in a well defined volume because ions deposit most of their energy at the end of their range, forming a Bragg peak (Caruso & Pais, 1996). To date mainly three laser-ion acceleration mechanisms have been demonstrated, i.e., the target-normal sheath acceleration (Cowan *et al.*, 2004), the break-out afterburner (BOA) (Yin *et al.*, 2006; Hegelich *et al.*, 2006), and the radiation pressure acceleration (RPA) (Esirkepov *et al.*, 2004; Henig *et al.*, 2009).

In target-normal sheath acceleration, the ponderomotive force of the laser provides thermal clouds of electrons and a strong charge-separation field to accelerate ions. This process can be described by the model of free plasma expansion into vacuum (Mora, 2003). The density of target-normal sheat acceleration ions is too low (usually less than the critical density n_c) for many applications, such as for research in high energy-density matter (HEDM) (Patel *et al.*, 2003) and fast ignition (FI) (Roth *et al.*, 2001). To increase the density of the ion beams, the rear surface can be tailored to a spherical curvature in order to ballistically focus these protons to a small spot (Patel *et al.*, 2003; Roth *et al.*, 2001; Wilks *et al.*, 2001). Using a spherically shaped target, a focused proton

Address correspondence and reprint requests to: Jie Liu, Institute of Applied Physics and Computational Mathematics, Beijing 100088, China. E-mails: liu_jie@iapcm.ac.cn; steelan_liu@yahoo.com

beam is produced and used to heat a smaller volume to over 20 eV, which provides a unique method for creating isochorically heated high-energy density plasma states (Patel *et al.*, 2003).

Based on particle-in-cell (PIC) simulations, the generation of proton beams using a target with a concave back surface was first studied by Wilks *et al.* (2001). They found that protons can be focused to a spot with high energy density. Following this work, a comprehensive study of the dependence of the maximum proton energy on different (concave) target shapes has been presented by Okada *et al.* (2006), which concluded that a parabolic concave target is optimal for proton acceleration. By using a thin parabolic concave target, the maximum ion energy is greatly enhanced, and an optimum width for generating a high-quality ion bunch exists (Liu *et al.*, 2008). *Via* adding an axial filament stemming to the apex of a cone cavity (umbrella-like cavity target), it is found that instead of diverging after first focusing, as in the cone-shaped target, the protons produced from the umbrella-like target are well collimated (Ma *et al.*, 2009).

In this paper, we develop a simple fluid theory based on the charge-separation field to investigate the physical mechanism behind the ion jet generation. We find that the emergence of the ion jet is accompanied by a dramatic distortion of the expanding ion surface. We have obtained analytical expressions for the time when the ion jet emerges and the maximum velocity that the ion jet acquires. Our theoretical analysis has been verified by PIC simulations. Our paper is organized as follows: In Section 2, we analyze the dynamics of concave target irradiated by laser pulse. Based on an extended ion expanding model, we present our analytical results on ion jet generation. To confirm the theoretical estimates, we carry out a 2D3V PIC simulations in Section 3. The PIC simulations show a clear signal of ion jet generation. Our theoretical analyses are supported by the simulation results. Section 4 is the conclusion.

2. THE DYNAMICS OF THE ION EXPANDING MODEL

An ultraintense laser incident on a target accelerates a large number of electrons. These electrons propagate to the rear side of the typical thin foil target and produce a charge-separation field. The ion acceleration on the rear surface could be explained by the model of self-similar plasma expansion into vacuum (Mora, 2003). In the expansion process, an ion layer with thickness of the Debye length λ_D on the ion expanding surface is accelerated by a time-dependent charge-separation field. Now we focused on the dynamics of the thin layer. In contrast to previous work (Mora, 2003), we extend our analysis to a 2D configuration, and the laser is propagates along x direction. Essentially, the charge-separation field E_f on the layer is position-independent, pointing normal to the rear surface.

The ion expansion is commonly described by the simple self-similar, isothermal, fluid model (Mora, 2003; Fuchs *et al.*, 2006), in which the electrostatic charge-separation field is given by

$$E_f \simeq \frac{\sqrt{2/e}E_0}{\sqrt{1+\tau^2}}, \tag{1}$$

where $E_0 = \sqrt{n_{e0}k_BT_h/\epsilon_0}$, $\tau = \omega_{pi}^2(t-t_0)^2/(2e)$, and $\omega_{pi} = \sqrt{Zq^2n_{e0}/m_i\epsilon_0}$ is the ion plasma frequency, with e being the exponential constant, m_i being the ion mass, q being the electron charge, ϵ_0 being the electric permittivity, Z being the charge number, T_h and n_{e0} the are temperature and density of the hot electrons that drive the rear-surface expand, t_0 is the time when the rear surface begins to expand. Then the equations of motion for an element on the layer become

$$\begin{aligned}\frac{\partial^2 x}{\partial t^2} &= \frac{q_i}{m_i}E_f\frac{\partial y}{\partial s},\\ \frac{\partial^2 y}{\partial t^2} &= -\frac{q_i}{m_i}E_f\frac{\partial x}{\partial s},\end{aligned} \tag{2}$$

where q_i is the ion charge, and $ds = (dx^2+dy^2)^{1/2}$ is the length of the surface element. These equations coincide with Ott's (1972) equations.

We set the initial front surface of the target at X. We immediately see that a one-dimension-fit carried out by Mora (2003)

$$x_0 = X + 2\sqrt{2e}\lambda_{D0}\left(\tau\ln\left(\tau+\sqrt{\tau^2+1}\right)-\sqrt{\tau^2+1}+1\right), \tag{3}$$

$$y_0 = s, \tag{4}$$

is a trivial solution, and indeed this is just the unperturbed equilibrium, where $\lambda_{D0} = \sqrt{\epsilon_0k_BT_h/(n_{e0}q^2)}$ is the Debye length when the rear surface begins to expand. The most general solution of Eq. (2) is

$$x = x_0 - \sum_{k,\sigma}\xi_x^{\sigma}(k,t)\cos(ks+\theta_k^{\sigma}), \tag{5}$$

$$y = y_0 - \sum_{k,\sigma}\xi_y^{\sigma}(k,t)\sin(ks+\theta_k^{\sigma}), \tag{6}$$

where $\xi_{x,y}^{\sigma}(k,t)$ satisfy

$$\ddot{\xi}_{x,y}^{\sigma} - \frac{kq_iE_f}{m_i}\xi_{y,x}^{\sigma} = 0, \tag{7}$$

and σ labels the independent solutions of Eq. (7). By assuming $E_f(t)$ changes slow, and neglecting the oscillating and dumping roots, we look for a Wentzel-Kramers-Brillouin solution of the form

$$\xi_x = \xi_y = a\cosh(\Phi(t)), \tag{8}$$

where $\Phi(t) = \int_{t_0}^{t}\sqrt{kq_iE_f(t')/m_i}dt'$, a and k denote the amplitude and circular wavenumber of the perturbation,

https://doi.org/10.1017/S0263034610000303 Published online by Cambridge University Press

respectively. Since the solution Eqs. (5), (6) is nonlinear (Ott, 1972), we look at a special case for a given k component to consider the solution in more detail

$$x = X + 2\sqrt{2e}\lambda_{D0}\left(\tau \ln\left(\tau + \sqrt{\tau^2+1}\right) - \sqrt{\tau^2+1} + 1\right) - a\cosh(\Phi(t))\cos ks, \tag{9}$$

$$y = s - a\cosh(\Phi(t))\sin ks. \tag{10}$$

This solution extends the expanding model by adding a 2D-perturbation to a semi-empirical/analytical 1D solution of Mora (2003). For arbitrary amplitudes, Eqs. (9)–(10) are actually the parametric representation of a cycloid (i.e., the path followed by a point on the surface of a rolling wheel). When $t = 0$ the rear-side shape of the target is set to

$$y = \frac{1}{k}\arccos\left(-\frac{x-X}{a}\right) - a\sin\left(\arccos\left(-\frac{x-X}{a}\right)\right). \tag{11}$$

The time evolution of the profile of the ion expanding surface is shown in Figure 1. Apparently, the above analysis is valid for $ka < 1$. At $t = 0$, when a is small, the curve is approximately sinusoidal, $x \approx X - a\cos(ky)$; at $0 < t < t^*$, the sinusoidal shape has become distorted; at $t = t^*$ a cusp develops in the curve; and at $t > t^*$ the solution Eqs. (9)–(10) are not valid any more because the analytical model breaks down past the cusp. The critical time t^* is solved in the following.

Now we restrict our analysis to $t < t^*$. From Eqs. (9)–(10), we obtain the ion velocity on the expanding surface (Mora, 2003)

$$v_{e,x} = 2c_s \ln\left(\tau + \sqrt{\tau^2+1}\right) - a\sqrt{kg(t)}\sinh(\Phi(t))\cos ks, \tag{12}$$

$$v_{e,y} = -a\sqrt{kg(t)}\sinh(\Phi(t))\sin ks. \tag{13}$$

where $g(t) = q_i E_f(t)/m_i$, and $c_s = \sqrt{Zk_BT_h/m_i}$ is the ion-acoustic velocity. The transverse velocity on the expanding surface $v_{e,y}$ is shown in Figure 2. Initially, the profile of the transverse ion velocity in the phase space is approximately a sinusoidal wave. With time increasing, the profile becomes more distorted. This means that the ions on the surface are focused to the central axis, which is confirmed by the following analysis.

The ion density of the expanding surface is dependent on the velocity *via* the equation of continuity

$$\frac{d}{dt}n_i + n_i\left(\frac{\partial v_x}{\partial x} + \frac{\partial v_y}{\partial y}\right) = 0. \tag{14}$$

According to Eq. (13), we have

$$\frac{\partial v_y}{\partial y} = \simeq \frac{\partial v_{e,y}}{\partial y} = \frac{\partial v_{e,y}}{\partial s}\Big/\frac{\partial y}{\partial s} = = -\frac{ka\sqrt{kg(t)}\sinh(\Phi(t))\cos ks}{1 - ka\cosh(\Phi(t))\cos ks}. \tag{15}$$

In the longitudinal direction, it is suitable to describe the expanding process by the one-dimension model. Then the ion density becomes

$$n_i = n_{ip}\frac{1 - ka\cos ks}{1 - ka\cosh(\Phi(t))\cos ks}, \tag{16}$$

where $n_{ip} = 2n_{i0}/(e(1+\tau^2))$ is the ion density at the expanding surface for the plane target (Mora, 2003), $n_{i0} = n_{e0}/Z$ is the initial ion density of the sheath. There is a singularity when the denominator is zero. For $s = 0$, we obtain the critical time t^* in the implicit form

$$ka\cosh(\Phi(t^*)) = 1. \tag{17}$$

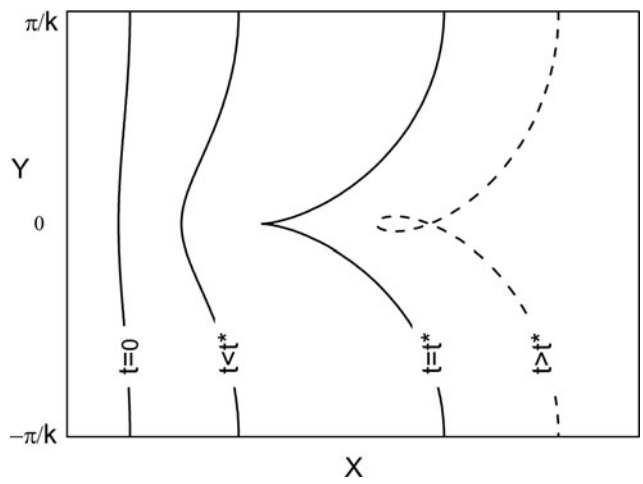

Fig. 1. Schematic of the time evolution of the profile of the ion expanding surface.

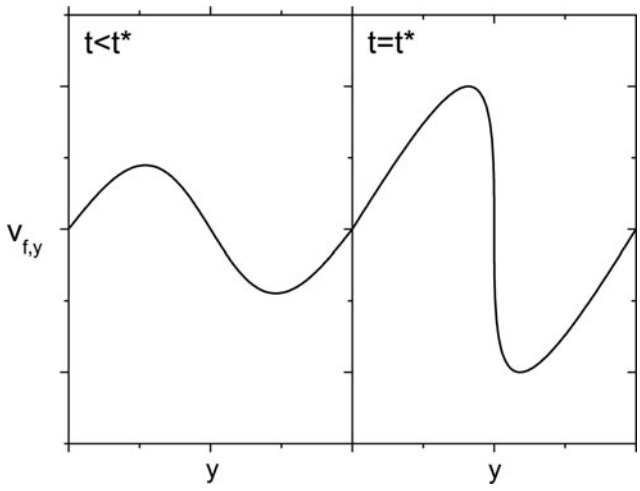

Fig. 2. The transverse velocity on the expanding surface in the phase space by combining Eq. (10) and Eq. (13).

https://doi.org/10.1017/S0263034610000303 Published online by Cambridge University Press

This means that the ion density increases dramatically when the evolution time closes to t^*.

The increase of the ion density on the central axis of the expanding surface makes the electrostatic field at this point more strong than that off the central axis (confirmed by the PIC simulation in the next section). Ions are pushed by the strong electrostatic field from the central axis of the expanding surface toward the background electrons, then an ion jet is generated, and the surface is broken and a cusp emerges. When the focusing and jet formation of ions come to balance, in the motion frame (moving together with the surface), the expanding ion surface becomes approximately steady, and the ion velocities along the surface should be approximately equal because the electrostatic field is perpendicular to the surface. This assumption is valid when the intensity of laser below relativistic regime, and the plasma could be treated as fluid. Then we predict the maximum longitudinal velocity when $t > t^*$,

$$v = v_p + \sqrt{\left(\frac{\partial x_1}{\partial t}\right)^2 + \left(\frac{\partial y_1}{\partial t}\right)^2}\Bigg|_{t=t^*} = v_p + a\sqrt{kg(t^*)}\sinh(\Phi(t^*)), \tag{18}$$

where

$$v_p = 2c_s \ln\left(\frac{\omega_{pi}t}{\sqrt{2e}} + \sqrt{\frac{\omega_{pi}^2 t^2}{2e} + 1}\right) \tag{19}$$

is the maximum velocity of a planar target.

Simple analytical expressions can be derived from the Eqs. (17) and (18) in the asymptotic limit, $\tau \gg 1$. In this limit, $E_f \approx 2E_0/(\omega_{pi}t)$, and $\Phi(t) = \sqrt{8kc_s}(\sqrt{t} - \sqrt{t_0})$, $\cosh(\Phi(t)) \simeq \sinh(\Phi(t)) \simeq \exp(\Phi(t))/2$. Then from Eq. (17) and Eq. (18) we obtain the critical time

$$t^* = \left(\frac{1}{\sqrt{8kc_s}}\ln\left(\frac{2}{ka}\right) + \sqrt{t_0}\right)^2, \tag{20}$$

and the maximum ion velocity when $t > t^*$

$$v = v_p + \frac{4c_s\sqrt{1-k^2a^2}}{\ln\left(\frac{2}{ka}\right)}. \tag{21}$$

The above analysis is exact valid for the concave cavity shaped as Eq. (11), and it can be applied to other shapes of cavity approximately. As an example, we consider three kinds of special concave targets, circle, parabolic, and triangle, which have been discussed (Okada *et al.*, 2006) comprehensively. The cavity are defined as $x = f^c(y) = D\sqrt{1 - \frac{4y^2}{W^2}}$, $x = f^p(y) = D\left(1 - \frac{4y^2}{W^2}\right)$, and $x = f^t(y) = D\left(1 - \left|\frac{2y}{W}\right|\right)$, where f^c, f^p, f^t denote circle, parabolic and triangle cavity, respectively, D is the depth and W is the diameter of the cavity. Now we expand the curve into the Fourier series. We have $a_n = \frac{2}{W}\int_{-W/2}^{W/2} f(y)\cos\frac{2\pi ny}{W}$. Since the long-wavelength components tend to dominate the ion jet at long time (Ott, 1972), we analyze the jet generation from the first order term. The first order terms are $a_1^{p,t} = 4D/\pi^2$ and $a_1^c = DJ_1(\pi) \sim |a_1^{p,t}|$. It means that there are little differences. Then, we consider the second order terms. Since $a_2^t = 0$, $a_2^p = -D/\pi^2$, and $a_2^c = DJ_1(2\pi)/2 \sim a_2^p$, it is less efficient to generate an ion jet from the rear-side of the trianglar concave target because of the missing second order perturbation. Hence, the maximum ion velocity of the trianglar concave target will be less than the other two kinds of targets. This simple analysis agrees with the simulation results (Okada *et al.*, 2006).

3. PIC SIMULATION

To confirm the above estimates, we carried out our PIC simulations with the 2D3V VORPAL code (Nieter & Cray, 2004). The schematic drawing of our simulations is shown in Figure 3. In a simulation box of $80 \times 30\ \mu m^2$ with a grid of 8000×1500 cells, a y direction linearly polarized laser pulse with central wavelength $\lambda = 1\ \mu m$ and peak intensity $I = 1.38 \times 10^{20}\ Wcm^{-2}$ is incident normal onto a target along the x (axial) direction. The target density is $10n_c$, where $n_c = m_e\epsilon_0\omega^2/q$ is the critical plasma density, with m_e the electron mass, $\omega = 2\pi c/\lambda$ the laser frequency, and c the velocity of light. The laser has a Gaussian envelope $A_y \sim A_0 \exp[-(\rho/\rho_0)^2 - (t/T_L)^2]$, with spot size $\rho_0 = 10\ \mu m$, and pulse width $L = cT_L$ is ranging from 30 μm to 100 μm, where A_0 is the vector potential, T_L denotes the laser pulse duration. The front surface of the target is located at $x = 30\ \mu m$. The origin of the coordinate system is $x = 0\ \mu m$, $y = -15\ \mu m$. The transverse and longitudinal boundary conditions are periodic and absorbing, respectively. The target, with 30 μm in width and $d = 10\ \mu m$ in thickness, has a cavity on the rear surface. The geometry of

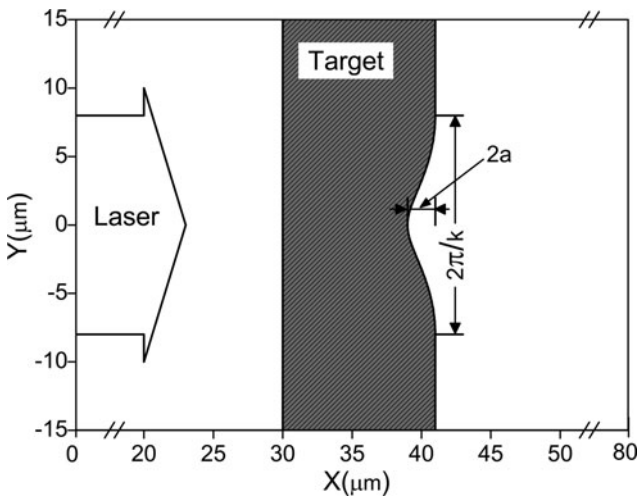

Fig. 3. Schematic drawing of the simulation box.

https://doi.org/10.1017/S0263034610000303 Published online by Cambridge University Press

the cavity is given by Eq. (11), where $X = 40$ μm, $2\pi/k = 16$ μm. At the beginning of simulations, i.e., $t = 0$, the peak of the laser pulse is at $x = -L$ and reaches the target surface at $t_0 = 30\lambda/c + T_L$. The ion/electron mass ratio is $m_i/m_e = 1836$ and the charge number $Z = 1$. The transverse and longitudinal boundary conditions are periodic and absorbing, respectively. The initial electron and ion temperatures are assumed to be small and their effects can be ignored. When an ultraintense laser pulse irradiates a plasma target, the temperature of the laser-driven hot electrons T_h is found numerically and experimentally to be given by the laser ponderomotive potential (Wilks *et al.*, 1992; Malka & Miquel, 1996),

$$k_B T_h = m_e c^2 \left(\sqrt{1 + \frac{I\lambda^2}{1.37 \times 10^{18} W\,\mu m^2/cm^2}} - 1 \right). \qquad (22)$$

The total number of electrons accelerated into the target is $N_e = f\varepsilon_L/T_h$, where ε_L is the laser energy, and $f = 1.2 \times 10^{15} I^{0.74}$ (Wcm^2) with saturation of 0.5 is the converted fraction from laser energy to hot electrons (Key *et al.*, 1998; Feurer *et al.*, 1997).

Figures 4 and 5 show that the ion density and the axial electric field E_x spatial distribution at $t = 90\lambda/c$ for $a = 1$ μm, respectively. In this simulation, the critical time is $t^* = 83\lambda/c$, and hence, the figure shows the spatial distribution after the critical time. In Figure 5, a strong charge-separation field at the front of the expanding surface is clearly shown. Figure 6 presents the comparison between the electric field E_x on the cental axis and that off the central axis. It is shown that the electric field on the central axis is a stronger than that off the cental axis, and the ion expanding surface is distorted by the strong electric field with a singular cusp shown on the central axis. As expected, a forward ion jet emerges from the central axis of the ion expanding surface.

Figure 7 presents the ion velocity distribution. The left column subfigures (the longitudinal velocity) show that the ions extracted from the rear-side of the target are accelerated forward. The maximum axial velocity of the ions is located at

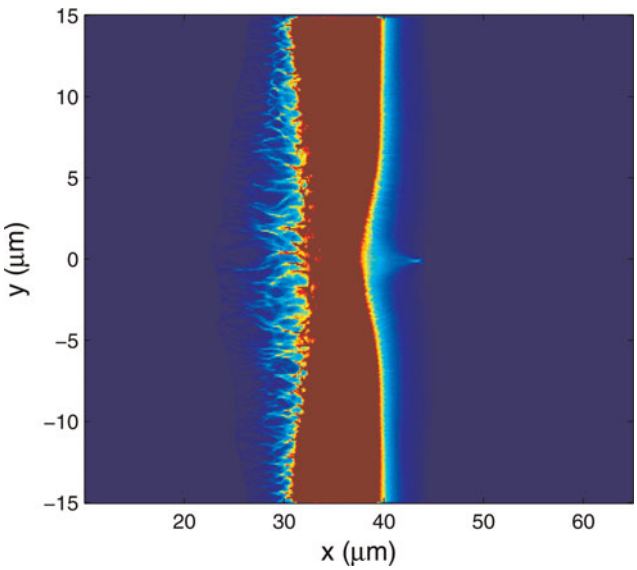

Fig. 4. (Color online) The ion density spatial distribution at $t = 90\lambda/c$ for $a = 1$ μm. It is shown that an ion jet is generated.

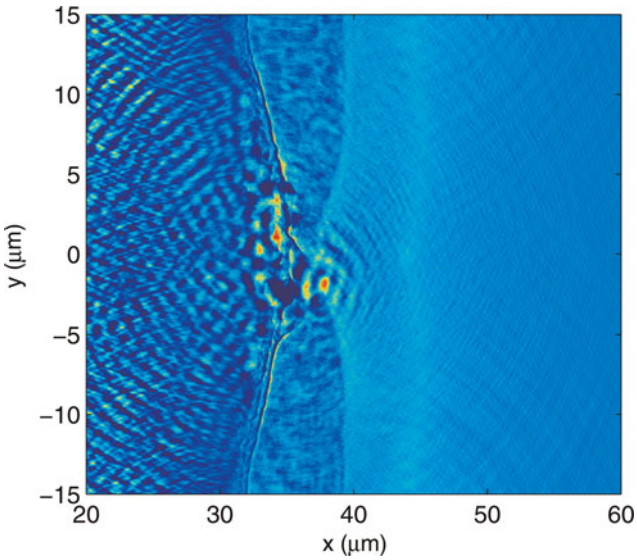

Fig. 5. (Color online) The axial electric field E_x spatial distribution at $t = 90\lambda/c$ for $a = 1$ μm. A bright thin layer in front of the target denotes the electric field at the ion expanding surface E_f.

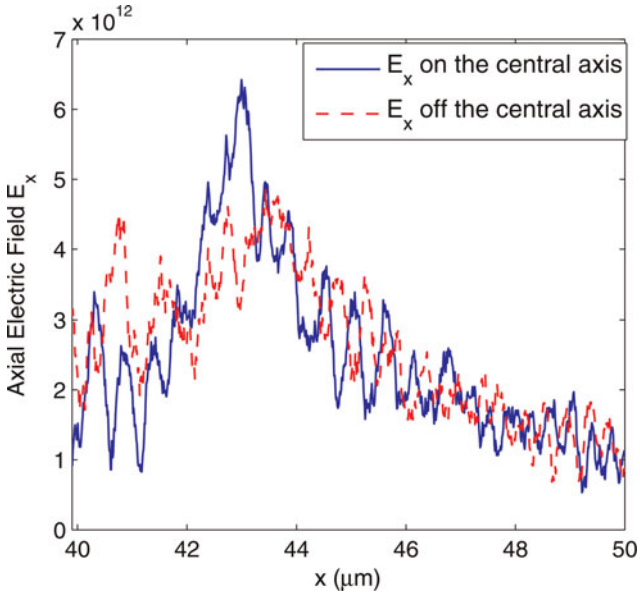

Fig. 6. (Color online) Comparison of the axial electric field E_x at $t = 90\lambda/c$ for $a = 1$ μm. The solid (blue) line denotes the electric field on the central axis ($y = 0$ μm), and the dashed (red) line denotes the electric field off the central axis ($y = 3$μm).

https://doi.org/10.1017/S0263034610000303 Published online by Cambridge University Press

the leading edge of the expanding ion surface on the central axis represented by a sharp peak in left column subfigures. The right column subfigures (the transverse velocity) verify our theoretical analysis in Figure 2. When $t = 40\lambda/c$, the transverse velocity distribution shows a sinusoidal wave profile, while when $t = 70\lambda/c$, the profile becomes more distorted.

Figure 8 shows the relative ion density n_i/n_{ip} as a function of time. The simulation data agree well with the theoretical results Eq. (16). Initially, the relative ion density is about one. In the region of a anticipated asymptotic value of time t_{max}, the relative ion density increases dramatically and closes to a saturation. This means that the focusing and jet formation of ions come to balance, and the forward ion jet will persist for a long time.

Figure 9 shows the PIC simulation results of maximum ion velocity as a function of time both for a concave target with $a = 1$ μm and planar target with $a = 0$. There is a clear indication of the post-accelerating at the time interval $(60\lambda/c, 80\lambda/c)$. Note that according to our model, when $t^* = 83\lambda/c$, the post-accelerated ions form an ion jet. Our model predicts that the velocity difference between the concave and the planar target is about 1.7×10^7 m/s, close to the simulation results 2.1×10^7 m/s.

Now we simulate the ion jet generation for different initial perturbation amplitudes a. Figure 10 shows the simulation results of the critical time for different a after irradiation by a plane-wave laser initially located at $x = 0$. With a increasing, the critical time decreases to t_0. In our simulation, the critical time is marked by the time when n_i/n_{ip} exceeds 10. The factor 10 is motivated by the analysis of the results described in Figure 8. Eq. (17) is solved by numerical method and the electrostatic field E_f is determined by

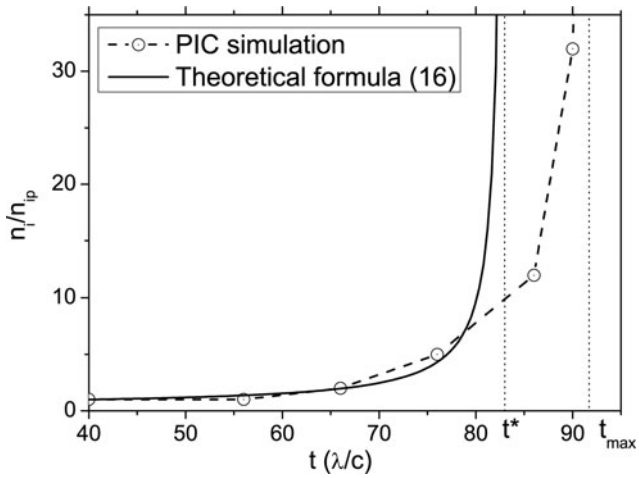

Fig. 8. Relative ion density n_i/n_{ip} as a function of time for concave target with $a = 1$ μm. In the region of a anticipated asymptotic value of time t_{max}, the relative ion density increases dramatically and closes to a saturation. The solid line is our analytical predict according to Eq. (16)

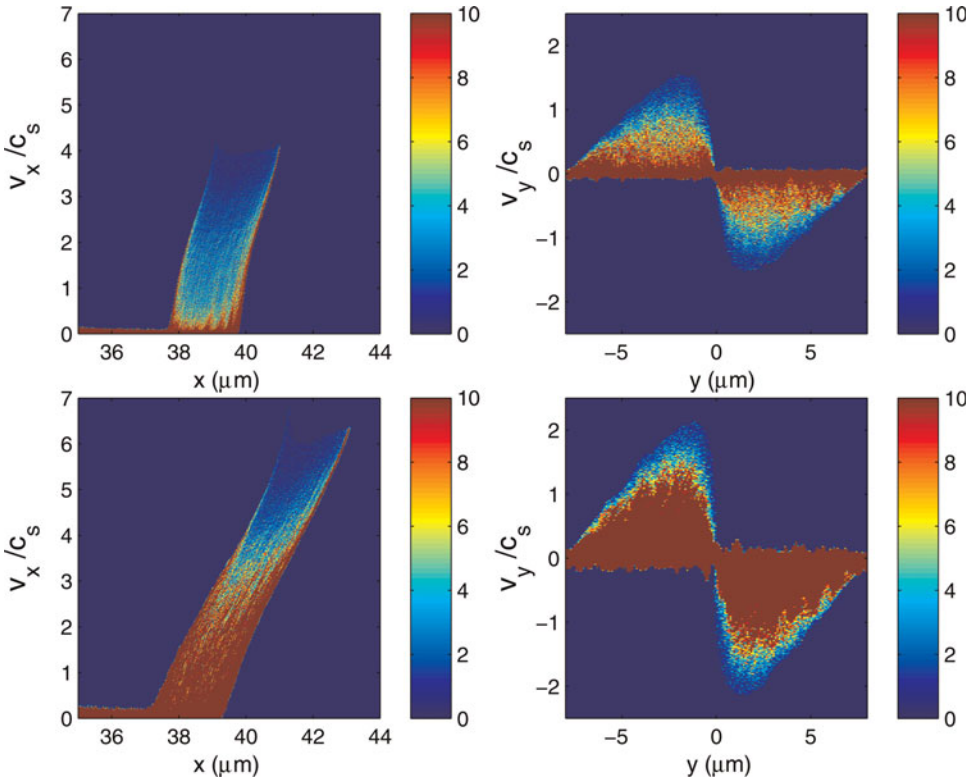

Fig. 7. (Color online) Time evolution and ion phase space distributions of the longitudinal (left column) and the transverse (right column) direction at $t = 40\lambda/c$ (top row) and $t = 70\lambda/c$ (bottom row), by simulating a concave target with $a = 1$μm.

https://doi.org/10.1017/S0263034610000303 Published online by Cambridge University Press

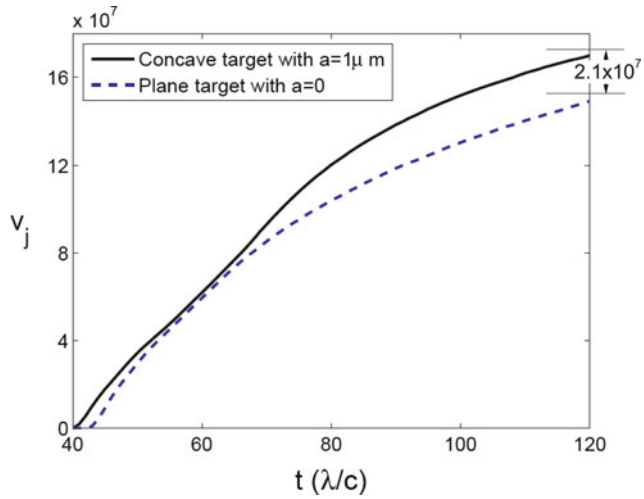

Fig. 9. The maximum velocity as a function of time for $a = 1$ μm.

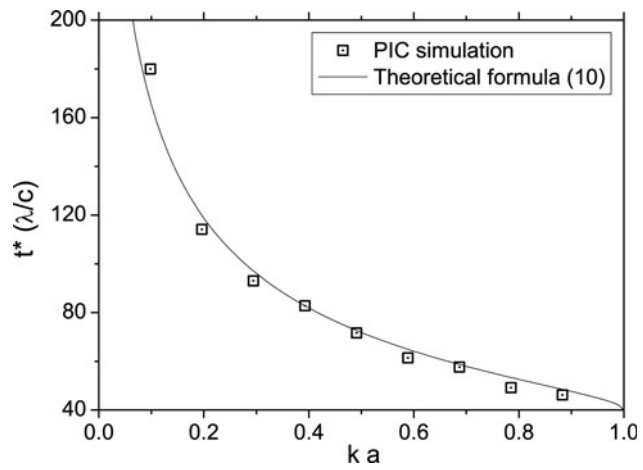

Fig. 10. The critical time for different *a*after irradiation by a plane-wave laser initially located at $x = 0$. In the simulation, the critical time is marked by the time when n_i/n_{ip} exceeds 10. The factor 10 is motivated by the analysis of the results described in Figure 8.

Eq. (1) as an approximation. The results of the simulation and the predicted curve according to Eq. (17) agree very well.

Figure 11 presents the maximum ion velocity for different a. The cut-off acceleration time is assumed to be $t = 1.3T_L$ (Fuchs *et al.*, 2006) with pulse width $L = cT_L = 100$ μm. There is a big difference between our prediction and simulation results when $ka \sim 1$. The main reason is that, for $ka > 0.5$, the simulation time is much greater than the jet generation time, and the ion jet will be defocused. This means that, the short-wavelength perturbations have little contribution to the collimated ion jets. Then we can conclude that, $ka = 0.5$ is the optimal parameter to generate the high collimated ion jet.

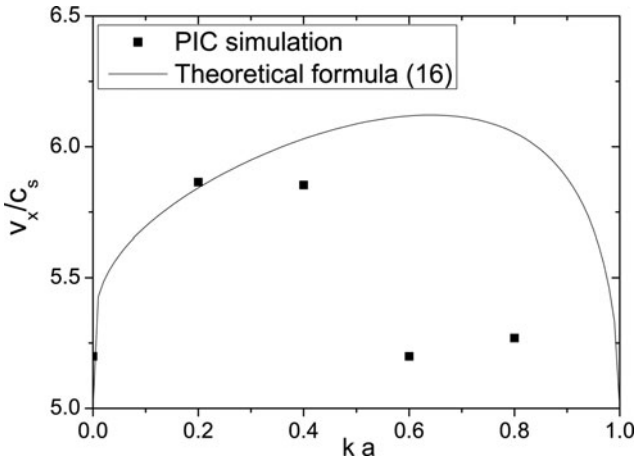

Fig. 11. The maximum velocity for different shapes. The effective acceleration time in the calculation is selected as $1.3T_L$ with pulse width $L = cT_L = 100$ μm.

4. CONCLUSION

In this paper, we investigated the interaction of an ultraintense laser pulse and a rear-side concave target using both a theoretical model and PIC simulations. It is shown that the emergence of an on-axis ion jet at the rear-side of the target is accompanied by a distorted, expanding ion surface. This distortion is caused by the strong charge-separation field. We presented a critical time, at which the distortion becomes dramatic with a singular cusp shown on the central axis. Meanwhile, the variation of the transverse ion velocity and the relative ion density diverge on the cusp, signaling the emergence of an on-axis ion jet. We obtained analytical expressions for the critical time and the maximum velocity of the ion jet, and suggested an optimum shape for generating a collimated energetic ion jet. Our PIC simulations support the theoretical analysis. Our results are useful in the design of target used in producing highly collimated energetic ions in high-energy-density physics.

ACKNOWLEDGMENTS

This work is supported by the National Fundamental Research Programme of China (Contact Nos.2007CB815103, 2007CB814800), the National Natural Science Foundation of China (Contact Nos. 10725521, 10875015, 10834008), and the Foundation of CAEP (Contact No. 2006Z0202).

REFERENCES

Bulanov, S.V. & Khoroshkov, V.S. (2002). Feasibility of using laser ion accelerators in proton therapy. *Plasma Phys. Rep*. **28**, 453–456.

Caruso, A. & Pais, V.A. (1996). The ignition of dense DT fuel by injected triggers. *Nucl. Fusion* **36**, 745–758.

Cowan, T.E., Fuchs, J., Ruhl, H., Kemp, A., Audebert, P., Roth, M., Stephens, R., Barton, I., Blazevic, A., Brambrink, E., Cobble,

https://doi.org/10.1017/S0263034610000303 Published online by Cambridge University Press

J., Fernández, J., Gauthier, J.-C., Geissel, M., Hegelich, M., Kaae, J., Karsch, S., Le sage, G.P., Letzring, S., Manclossi, M., Meyroneinc, S., Newkirk, A., Pépin, H. & Renard-Legalloudec, N. (2004). Ultralow emittance, Multi-MeV proton beams from a laser virtual-cathode plasma accelerator. *Phys. Rev. Lett*. **92**, 204801.

Dromey, B., Bellei, C., Carroll, D.C., Clarke, R.J., Green, J.S., Kar, S., Kneip, S., Markey, K., Nagel, S.R., Willingale, L., McKenna, P., Neely, D., Najmudin, Z., Krushelnick, K., Norreys, P.A. & Zepf, M. (2009). Third harmonic order imaging as a focal spot diagnostic for high intensity laser-solid interactions. *Laser Part. Beams* **27**, 243–248.

Esirkepov, T., Borghesi, M., Bulanov, S.V., Mourou, G. & Tajima, T. (2004). Highly efficient relativistic-ion generation in the laser-piston regime. *Phys. Rev. Lett*. **92**, 175003.

Fazio, E., Neri, F., Ossi, P.M., Santo, N. & Trusso, S. (2009). Ag nanocluster synthesis by laser ablation in Ar atmosphere: A plume dynamics analysis, laser and particle beams. *Laser Part. Beams* **27**, 281–290.

Feurer, T., Theobald, W., Sauerbrey, R., Uschmann, T., Altenbernd, D., Teubner, U., Gibbon, P., Förster, E., Malka, G. & Miquel, J.L. (1997). Onset of diffuse reflectivity and fast electron flux inhibition in 528-nm-laser-solid interactions at ultrahigh intensity. *Phys. Rev. E* **56**, 4608–4614.

Fuchs, J., Antici, P., D'humières, E., Lefebvre, E., Borghesi, M., Brambrink, E., Cecchetti, C.A., Kaluza, M., Malka, V., Manclossi, M., Meyroneinc, S., Mora, P., Schreiber, J., Toncian, T., Pépin, H. & Audebert, P. (2006). Laser-driven proton scaling laws and new paths towards energy increase. *Nat. Phys*. **2**, 48–54.

Glowacz, S., Hora, H., Badziak, J., Jablonski, S., Cang, Y. & Osman, F. (2006). Analytical description of rippling effect and ion acceleration in plasma produced by a short laser pulse. *Laser Part. Beams* **24**, 15–22.

Hegelich, B.M., Albright, B.J., Cobble, J., Flippo, K., Letzring, S., Paffett, M., Ruhl, H., Schreiber, J., Schulze, R.K. & Fernández, J.C. (2006). Laser acceleration of quasi-monoenergetic MeV ion beams. *Nat*. **439**, 441–444.

Henig, A., Steinke, S., Schnürer, M., Sokollik, T., Hörlein, R., Kiefer, D., Jung, D., Schreiber, J., Hegelich, B.M., Yan, X.Q., Meyer-ter-Vehn, J., Tajima, T., Nickles, P.V., Sandner, W. & Habs, D. (2009). Radiation-pressure acceleration of ion beams driven by circularly polarized laser pulses. *Phys. Rev. Lett*. **103**, 245003.

Hoffmann, D.H.H. (2008*a*). Laser interaction with matter and heavy ion fusion. *Laser Part. Beams* **26**, 509–510.

Hoffmann, D.H.H. (2008*b*). Laser matter interaction and related conferences. *Laser Part. Beams* **26**, 137–138.

Hong, W., He, Y., Wen, T., Du, H., Teng, J., Qing, X., Huang, Z., Huang, W., Liu, H., Wang, X., Huang, X., Zhu, Q., Ding, Y. & Peng, H. (2009). Spatial and temporal characteristics of X-ray emission from hot plasma driven by a relativistic femtosecond laser pulse. *Laser Part. Beams* **27**, 19–26.

Hora, H. (2007). New aspects for fusion energy using inertial confinement. *Laser Part. Beams* **25**, 37–45.

Izgorodin, V.M., Abzaev, F.M., Balyaev, A.P., Bessarab, A.V., Cherkesova, I.N., Chulkov, V.U., Fenoshin, D.Y., Garanin, S.G., Gogolev, V.G., Golubinsky, A.G., Ignat'ev, Y.V., Irinichev, D.A., Lachtikov, A.E., Morovov, A.P., Nazarov, V.V., Nikolaev, G.P., Pepelyaev, A.P., Pinegin, A.V., Rojz, I.M., Romaev, V.N., Solomatina, E.Y., Vasin, M.G. & Veselov, A.V. (2009). Target technology development for the research of high energy density physics and inertial fusion at the RFNC-VNIIEF. *Laser Part. Beams* **27**, 657–680.

Karsch, S., Habs, D., Schatz, T., Schramm, U., Thirolf, P.G., Meyer-ter-Vehn, J. & Pukhov, A. (1999). Particle physics with petawatt-class lasers. *Laser Part. Beams* **17**, 565–570.

Kasperczuk, A., Pisarczyk, T., Nicolai, P.H., Stenz, C.H., Tikhonchuk, V., Kalal, M., Ullschmied, J., Krousky, E., Masek, K., Pfeifer, M., Rohlena, K., Skala, J., Klir, D., Kravarik, J., Kubes, P. & Pisarczyk, P. (2009*a*). Investigations of plasma jet interaction with ambient gases by multi-frame interferometric and X-ray pinhole camera systems. *Laser Part. Beams* **27**, 115–122.

Kasperczuk, A., Pisarczyk, T., Demchenko, N.N., Gus'kov, S.Y., Kalal, M., Ullschmied, J., Krousky, E., Masek, K., Pfeifer, M., Rohlena, K., Skala, J. & Pisarczyk, P. (2009*b*). Experimental and theoretical investigations of mechanisms responsible for plasma jets formation at PALS. *Laser Part. Beams* **27**, 415–427.

Kawata, S., Kong, Q., Miyazaki, S., Miyauchi, K., Sonobe, R., Sakai, K., Nakajima, K., Masuda, S., Ho, Y.K., Miyanaga, N., Limpouch, J. & Andreev, A.A. (2005). Electron bunch acceleration and trapping by ponderomotive force of an intense short-pulse laser. *Laser Part. Beams* **23**, 61–67.

Key, M.H., Cable, M.D., Cowan, T.E., Estabrook, K.G., Hammel, B.A., Hatchett, S.P., Henry, E.A., Hinkel, D.E., Kilkenny, J.D., Koch, J.A., Kruer, W.L., Langdon, A.B., Lasinski, B.F., Lee, R.W., Macgowan, B.J., Mackinnon, A., Moody, J.D., Moran, M.J., Offenberger, A.A., Pennington, D.M., Perry, M.D., Phillips, T.J., Sangster, T.C., Singh, M.S., Stoyer, M.A., Tabak, M., Tietbohl, G.L., Tsukamoto, M., Wharton, K. & Wilks, S.C. (1998). Hot electron production and heating by hot electrons in fast ignitor research. *Phys. Plasmas* **5**, 1966–1972.

Kline, J.L., Montgomery, D.S., Rousseaux, C., Baton, S.D., Tassin, V., Hardin, R.A., Flippo, K.A., Johnson, R.P., Shimada, T., Yin, L., Albright, B.J., Rose, H.A. & Amiranoff, F. (2009). Investigation of stimulated Raman scattering using a short-pulse diffraction limited laser beam near the instability threshold. *Laser Part. Beams* **27**, 185–190.

Koyama, K., Adachi, M., Miura, E., Kato, S., Masuda, S., Watanabe, T., Ogata, A. & Tanimoto, M. (2006). Monoenergetic electron beam generation from a laser-plasma accelerator. *Laser Part. Beams* **24**, 95–100.

Laska, L., Badziak, J., Gammino, S., Jungwirth, K., Kasperczuk, A., Krasa, J., Krousky, E., Kubes, P., Parys, P., Pfeifer, M., Pisarczyk, T., Rohlena, K., Rosinski, M., Ryc, L., Skala, J., Torrisi, L., Ullschmied, J., Velyhan, A. & Wolowsk, J. (2007). The influence of an intense laser beam interaction with preformed plasma on the characteristics of emitted ion streams. *Laser Part. Beams* **25**, 549–556.

Li, L.M., Liu, L., Cheng, G.X., Xu, Q.F., Ge, X.J. & Wen, J.C. (2009). Layer structure, plasma jet, and thermal dynamics of Cu target irradiated by relativistic pulsed electron beam. *Laser Part. Beams* **27**, 497–509.

Lifshitz, A.F., Faure, J., Glinec, Y., Malka, V. & Mora, P. (2006). Proposed scheme for compact GeV laser-plasma accelerator. *Laser Part. Beams* **24**, 255–259.

Limpouch, J., Psikal, J., Andreev, A.A., Platonov, K.Y. & Kawata, S. (2008). Enhanced laser ion acceleration from mass-limited targets. *Laser Part. Beams* **26**, 225–234.

Liu, M.P., Wu, H.C., Xie, B.S., Liu, J., Wang, H.Y. & Yu, M.Y. (2008). Energetic collimated ion bunch generation from an ultraintense laser interacting with thin concave targets. *Phys. Plasmas* **15**, 063104.

Ma, Y.Y., Sheng, Z.M., Gu, Y.Q., Yu, M.Y., Yin, Y., Shao, F.Q., Yu, T.P. & Chang, W.W. (2009). High-quality MeV protons from laser interaction with umbrellalike cavity target. *Phys. Plasmas* **16**, 034502.

Malekynia, B., Ghoranneviss, M., Hora, H. & Miley, G.H. (2009). Collective alpha particle stopping for reduction of the threshold for laser fusion using nonlinear force driven plasma blocks. *Laser Part. Beams* **27**, 233–241.

Malka, G. & Miquel, L. (1996). Experimental confirmation of ponderomotive-force electrons produced by an ultrarelativistic laser pulse on a solid target. *Phys. Rev. Lett*. **77**, 75–78.

Malka, V. & Fritzler, S. (2004). Electron and proton beams produced by ultra short laser pulses in the relativistic regime. *Laser Part. Beams* **22**, 399–405.

Mangles, S.P.D., Walton, B.R., Najmudin, Z., Dangor, A.E., Krushelnick, K., Malka, V., Manclossi, M., Lopes, N., Carias, C., Mendes, G. & Dorchies, F. (2006). Table-top laser-plasma acceleration as an electron radiography source. *Laser Part. Beams* **24**, 185–190.

Mora, P. (2003). Plasma expansion into a vacuum. *Phys. Rev. Lett*. **90**, 185002.

Nieter, C. & Cray, J.R. (2004). VORPAL: A versatile plasma simulation code. *J. Comput. Phys*. **196**, 448–473.

Okada, T., Andreev, A.A., Mikado, Y. & Okubo, K. (2006). Energetic proton acceleration and bunch generation by ultraintense laser pulses on the surface of thin plasma targets. *Phys. Rev. E* **74**, 026401.

Ott, E. (1972). Nonlinear evolution of the Rayleigh-Taylor instability of a thin layer. *Phys. Rev. Lett*. **29**, 1429–1432.

Patel, P.K., Mackinnon, A.J., Key, M.H., Cowan, T.E., Foord, M.E., Allen, M., Price, D.F., Ruhl, H., Springer, P.T. & Stephens, R. (2003). Isochoric heating of solid-density matter with an ultrafast proton beam. *Phys. Rev. Lett*. **91**, 125004.

Roth, M., Brambrink, E., Audebert, B., Blazevic, A., Clarke, R., Cobble, J., Geissel, M., Habs, D., Hegelich, M., Karsch, S., Ledingham, K., Neelz, D., Ruhl, H., Schlegel, T. & Schreiber, J. (2005). Laser accelerated ions and electron transport in ultra-intense laser matter interaction. *Laser Part. Beams* **23**, 95–100.

Roth, M., Cowan, T.E., Key, M.H., Hatchett, S.P., Brown, C., Fountain, W., Johnson, J., Pennington, D.M., Snavely, R.A., Wilks, S.C., Yasuike, K., Ruhl, H., Pegoraro, F., Bulanov, S.V., Campbell, E.M., Perry, M.D. & Powell, H. (2001). Fast ignition by intense laser-accelerated proton beams. *Phys. Rev. Lett*. **86**, 436–439.

Sadighi-Bonabi, R., Navid, H.A. & Zobdeh, P. (2009). Observation of quasi mono-energetic electron bunches in the new ellipsoid cavity model. *Phys. Rev. Lett*. **27**, 223–231.

Sakai, K., Miyazaki, S., Kawata, S., Hasumi, S. & Kikuchi, T. (2006). High-energy-density attosecond electron beam production by intense short-pulse laser with a plasma separator. *Laser Part. Beams* **24**, 321–328.

Sharma, R.P. & Sharma, P. (2009). Effect of laser beam filamentation on second harmonic spectrum in laser plasma interaction. *Laser Part. Beams* **27**, 157–169.

Wilks, S.C., Kruer, W.L., Tabak, M. & Langdon, A.B. (1992). Absorption of ultra-intense laser pulses. *Phys. Rev. Lett*. **69**, 1383–1386.

Wilks, S.C., Langdon, A.B., Cowan, T.E., Roth, M., Singh, M., Hatchett, S., Key, M.H., Pennington, D., Mackinnon, A. & Snavely, R.A. (2001). Energetic proton generation in ultra-intense laser–solid interactions. *Phys. Plasmas* **8**, 542–549.

Yin, L., Albright, B.J., Hegelich, B.M. & Fernández, J.C. (2006). GeV laser ion acceleration from ultrathin targets: The laser break-out afterburner. *Laser Part. Beams* **24**, 291–298.

Yu, W., Xu, H., He, F., Yu, M.Y., Ishiguro, S., Zhang, J. & Wong, A.Y. (2005). Direct acceleration of solid-density plasma bunch by ultraintense laser. *Phys. Rev. E* **72**, 046401.

Yu, W., Yu, M.Y., Xu, H., Tian, Y.W., Chen, J. & Wong, A.Y. (2007). Intense local plasma heating by stopping of ultrashort ultraintense laser pulse in dense plasma. *Laser Part. Beams* **25**, 631–638.

https://doi.org/10.1017/S0263034610000303 Published online by Cambridge University Press